Journal of Nondestructive Evaluation (2020) 39:74
https://doi.org/10.1007/s10921-020-00722-0

Photothermal Porosity Estimation in CFRP by the Time-of-Flight of Virtual Waves

Holger Plasser[1] · Günther Mayr[1] · Gregor Thummerer[1] · Günther Hendorfer[1] · Peter Burgholzer[2] · Zoltán Major[3]

Received: 30 April 2020 / Accepted: 17 September 2020 / Published online: 24 September 2020

Abstract
Porosity is an unavoidable defect in carbon fiber reinforced polymers and has noticeable effects on mechanical properties since gas filled voids weaken the epoxy matrix. Pulsed thermography is advantageous because it is a non-contacting, non-destructive and fast photothermal testing method that allows the estimation of material parameters. Using the Virtual Wave Concept for thermography data, ultrasonic evaluation methods are applicable. In this work, the pulse-echo method for Time-of-Flight measurements is used, whereby the determined Time-of-Flight is directly related to the thermal diffusion time of the examined material. We introduce a signal-to-noise dependent approach, the optimum evaluation time, for evaluating only relevant time ranges which contain information of heat diffusion. After the validation of the method for heterogeneous materials, effective medium theories can be used for quantitative porosity estimation from the estimated diffusion time. This model-based approach for porosity estimation delivers more accurate results for transmission and reflection configuration measurements compared to thermographic state-of-the-art methods. The results are validated by X-ray computed tomography reference measurements on a wide range of different porous carbon fiber reinforced plastic specimens with different number of plies and varying porosity contents.

Keywords Active thermography · Photothermal technique · Virtual wave concept · Carbon fiber reinforced plastic · Heterogeneous material · Porosity estimation

1 Introduction

Porosity is an unavoidable defect in carbon fiber reinforced plastic (CFRP). It is caused by the formation of air-filled voids during the manufacturing process. Particularly, the autoclave molding of preimpregnated fibers (prepreg fabrics or unidirectional tapes) is a critical step in manufacturing. Enclosed air during the lay-up and insufficient hydrostatic pressure results to keep any moisture or volatiles dissolved in the resin until gelation occurs [1]. The aim is to reduce the porosity to a minimum using optimal process parameters. The presence of porosity has effects on the mechanical properties of the laminate since voids weaken the epoxy matrix. Especially, the matrix-dominated material properties, such as the transverse tensile strength and the interlaminar shear strength, decrease with increasing porosity [2,3]. In the production of safety-relevant CFRP components and structures, the characterization of porosity is indispensable and has to be characterized quantitatively with sufficient accuracy, e.g. in the aerospace industry a porosity content of lower than 2% is accepted for the most safety-critical parts. Balageas et al. [4] have shown the ability of active thermography for detection of defects with respect to variations in thermal properties. Since porosity has a measurable influence on the thermal diffusivity, former studies [5], based on the photothermal effect in transmission mode have been carried out for the estimation of porosity distribution in CFRP. Due to the strong dependence on the pore shape and distribution, the general properties of the microstructure (e.g. averaged pore shape and orientation) have to be known to allow the prediction

✉ Holger Plasser
holger.plasser@fh-wels.at

[1] Josef Ressel Center for Thermal NDE of Composites, University of Applied Sciences Upper Austria, Stelzhamerstraße 23, 4600 Wels, Austria

[2] Research Center for Non Destructive Testing (RECENDT), Altenbergerstraße 69, 4040 Linz, Austria

[3] Institute of Polymer Product Engineering (IPPE), Johannes Kepler University Linz, Altenbergerstraße 69, 4040 Linz, Austria

of the effective thermal diffusivity [6]. Based on effective medium theories (EMT), a sophisticated model was introduced by Mayr et al. [7]. This model enables the estimation of porosity in CFRP without the knowledge of the actual sample thickness, therefore the apparent thermal diffusivity is introduced and expressed as a quadratic model. Cernuschi [8] has shown the estimation of thermophysical properties by the use of thermographic techniques for thermal barrier coatings (TBC) with an overall uncertainty of ±5 % porosity. Currently, the precision of the porosity estimation based on the photothermal measurement of the thermal diffusion time is only appropriate for transmission measurements [6].

In this work, the quantitative non-destructive porosity estimation is also shown for reflection measurements with a comparable precision as in transmission mode. Due to the orthotropic stiffness of fabric CFRP, the specimen volume increases in out-of-plane direction, orthogonal to the layers, as a consequence of porosity. To determine this porosity dependent thickness increase and the simultaneously reduced thermal diffusivity, the Virtual Wave Concept (VWC) is applied. Former studies have shown the reliable parameter estimation by the VWC on homogeneous isotropic material [9]. For the first time, in this study the VWC concept is applied on heterogenous materials. The validation of the parameter estimation is shown on a CFRP step wedge and the ability to estimate porosity is shown on different porous CFRP test specimen (5-, 10- and 20-plies).

Heat diffusion causes entropy production that is equal to information loss. Hence, the transformation of the measured temperature signal to a virtual wave signal is a severely ill-posed inverse problem. To obtain an appropriate solution for this ill-posed inverse problem, we assume prior information in form of positivity and sparsity to overcome the diffusion based information loss, partly [10,11]. In order to evaluate only time ranges which contain information about the heat diffusion inside the sample a SNR dependent approach is introduced. Using this optimum evaluation time, in addition the undesired influence of heat losses due to convection are reduced. This enables a reliable quantitative porosity estimation for transmission and reflection measurements.

2 Virtual Wave Concept

In this work, we assume 1D heat diffusion for the following reasons:

- spatially homogeneous photothermal excitation of the surface by flash lamps
- plane-parallel CFRP test coupons with sufficient lateral expansion
- porous CFRP test coupons can be considered as an effective medium

To estimate the porosity-dependent thermal diffusion time $t_d = L^2\,\alpha^{-1}$, where α is the thermal diffusivity and L the sample thickness, the Virtual Wave Concept (VWC) is applied [12]. Trough the VWC, ultrasonic evaluation methods, are applicable on photothermal measurements. Therefore, a virtual wave field $T_{\mathrm{virt}}(\mathbf{r}, t')$ is calculated by applying a local transformation for the different timescales t and t' to the measurement data $T(\mathbf{r}, t)$. This transformation is a linear inverse problem and can be formulated as a Fredholm integral of the first kind

$$\int_{-\infty}^{\infty} K(t, t')T_{\mathrm{virt}}(\mathbf{r}, t')dt' = T(\mathbf{r}, t), \quad (1)$$

$$\text{with} \qquad K(t, t') = \frac{c}{\sqrt{\pi\alpha t}} \exp\left(-\frac{c^2 t'^2}{4\alpha t}\right) \text{ for } t > 0. \quad (2)$$

In our case the temperature distribution $T(\mathbf{r}, t)$ is obtained by a thermographic experiment. The kernel $K(t, t')$ is given exactly by the mathematical model of the virtual waves. α is the thermal diffusivity of the examined material and the virtual speed of sound c can be chosen arbitrarily.

2.1 Discretization

The sample surface temperature $T(\mathbf{r}, t)$ is measured with an infrared (IR) camera in reflection ($z = 0$) as well as in transmission mode ($z = L$). The temperature data T_k is pixel-wise recorded at many discrete time steps k starting simultaneous to the thermal stimulation ($t = 0$). The different discrete time scales are given by $t_k = (k-1)\Delta_t$ and $t'_j = (j-1)\Delta_{t'}$ with the running variables $k = (1, 2, \ldots, n)$ and $j = (1, 2, \ldots, m)$. In this work, we assume that the different time scales have equal time resolution ($\Delta_t = \Delta_{t'}$) and time steps ($n = m$). After discretization, Eq. 1 can be written in matrix form [11]:

$$\mathbf{T} = \mathbf{K}\mathbf{T}_{\mathrm{virt}} \xrightarrow[\text{notation}]{\text{component}} T_k = \sum_{j=1}^{n} K_{kj} T_{\mathrm{virt},j}. \quad (3)$$

Considering a 'Dirac-Delta' like heating function $h(t) = \delta(t)$, which is a good approximation for the flash light excitation, the components of the discrete kernel remain as follows:

$$K_{kj} = \frac{\tilde{c}}{\sqrt{\pi\,\Delta_{\mathrm{Fo}}(k-1)}} \exp\left(-\frac{\tilde{c}^2(j-1)^2}{4\Delta_{\mathrm{Fo}}(k-1)}\right) \quad (4)$$

with the dimensionless virtual speed of sound $\tilde{c}$ and the discrete Fourier number Δ_{Fo} [13]

$$\tilde{c} = \frac{c\Delta_{t'}}{\Delta_z}; \quad \Delta_{\mathrm{Fo}} = \frac{\alpha\Delta_t}{\Delta_z^2}. \quad (5)$$

Herein Δ_z denotes the spatial resolution.

2.2 Regularization with Prior Information

Entropy production during heat diffusion causes information loss [14,15]. Hence the calculation of the inverse of Eq. 3 is a discrete severely ill-posed inverse problem and regularization techniques are necessary to calculate an appropriate solution. To show the benefit of incorporating prior information, we compare the regularization techniques truncated singular value decomposition (T-SVD) and alternating direction method of multipliers (ADMM). For T-SVD, we only incorporate the knowledge about noise of the IR-camera detector as prior information. To include prior information in form of positivity and sparsity we use ADMM. Positivity is based on the assumption that the thermal wave and thus also the virtual wave propagates 1D. In analogy to the 1D photoacoustic wave, the 1D virtual wave includes only positive values [16]. Because of the effective medium assumption no intermediate echoes are expected in the sample. Consequently the virtual wave reflection occurs only at the front wall and back wall surface. In prior works we have shown that a Dirac-Delta like heating causes a Dirac-Delta like impulse response for the virtual wave [9]. Consequently we have a sparse signal that enables the incorporation of sparsity as prior information for regularization.

According to ADMM, we split the subsequent objective function into two parts [17]:

$$min \frac{1}{2} \left\| \mathbf{K}\mathbf{T}_{\text{virt}} - \mathbf{T} \right\|_2^2 + \lambda \left\| \mathbf{T}_{\text{virt}} \right\|_1 \tag{6}$$

Therefore, the new problem is given by:

$$min\ f(\mathbf{T}_{\text{virt}}) + g(\mathbf{z}) \tag{7}$$

with $f(\mathbf{T}_{\text{virt}}) = \frac{1}{2} \left\| \mathbf{K}\mathbf{T}_{\text{virt}} - \mathbf{T} \right\|_2^2$, $g(\mathbf{z}) = \lambda \left\| \mathbf{T}_{\text{virt}} \right\|_1$ and subject to

$$\mathbf{T}_{\text{virt}} = \mathbf{z}. \tag{8}$$

λ denotes the regularization parameter that is determined via the solution norm $\|\mathbf{T}_{\text{virt}}\|_1$ and residual norm $\|\mathbf{K}\mathbf{T}_{\text{virt}} - \mathbf{T}\|_2$. A good estimation for λ is found at the edge of the L-curve [18], as schematically illustrated in Fig. 1.

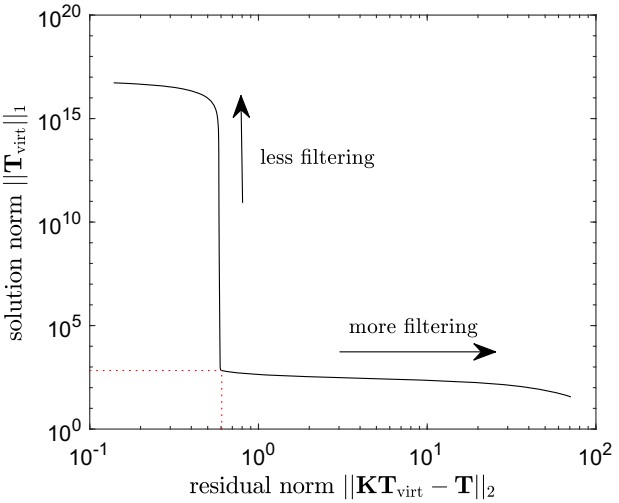

Fig. 1 The L-curve for ADMM regularization represents the solution norm $\|\mathbf{T}_{\text{virt}}\|_1$ as a function of the residual norm $\|\mathbf{K}\mathbf{T}_{\text{virt}} - \mathbf{T}\|_2$. A higher regularization parameter λ results in smoother solutions with more filtering

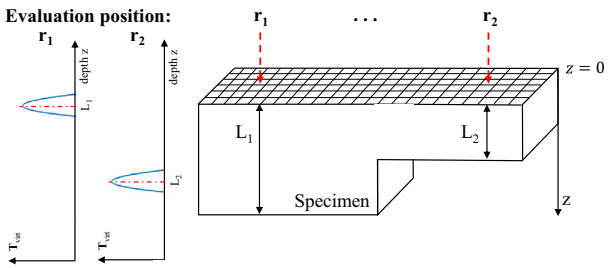

Fig. 2 A-Scan-at any discrete position $\mathbf{r}$

3 Estimation of the Thermal Diffusion Time

To estimate the thermal diffusion time t_{d}, we apply the Time-of-Flight (ToF) method from ultrasonic testing for the virtual wave data. After the absorption of optical radiation at the sample surface ($z = 0$), the calculated virtual wave originates and propagates into the specimen with a velocity c. For the visualization of the virtual wave, we use an A-Scan representation. The amplitude of the virtual wave field is displayed versus the time $t' = c^{-1} z$ [19]. By the arbitrarily chosen virtual speed of sound c, it is possible to estimate the thermal diffusion time by evaluating the time between the initial pulse $\delta(\text{t}_0)$ and the corresponding echo at the back surface $\delta(\text{t}_\text{L})$. Figure 2 shows the principle of the Time-of-Flight evaluation for two different positions on the test specimen by A-Scan representations. The point-wise evaluation allows a mapping of the diffusion time which could depend on spatially variations of the micro-structure, e.g. porosity, fiber density, degree of cure.

The mesh at $z = 0$, in Fig. 2, depicts the pixel or measurement points of the IR-camera. For each pixel we can calculate the ToF of the virtual wave signal for both transmission and reflection configuration.

The estimation of the thermal diffusion time via virtual wave signal and ToF is based on the 1D analytical solution of the heat conduction equation for adiabatic boundary conditions [20]. Here, a 'Dirac-Delta' like heating pulse $\delta(t)$ introduces the heat energy at $t = 0$ on the surface $z = 0$, yielding the initial condition (IC) $T_0(z, t = 0) =$

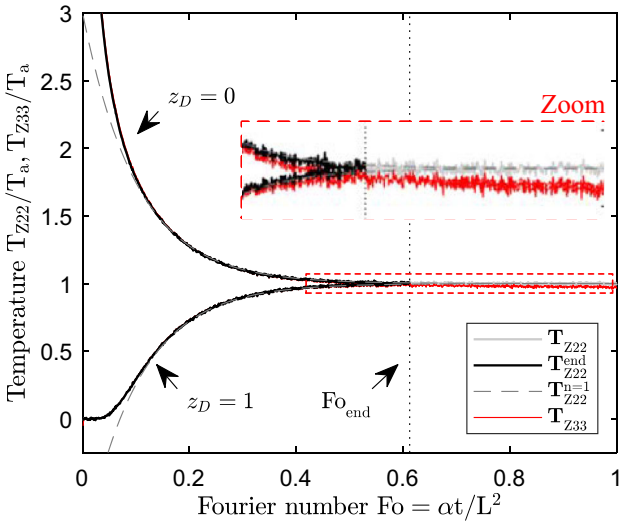

Fig. 3 Estimation of the optimum evaluation time. For this example, the Fo_{end} is 0.61. T_{Z22} and T_{Z33} distorted with additive white Gaussian noise (AWGN) with a standard deviation σ of 25 mK [21]

$q_0/(\rho c_p)\delta(z)$. Via the IC and the Greens function solution equation we can compute the corresponding temperature function:

$$T_{Z22}(z,t) = \frac{q_0}{\rho c_p L}\left(1 + 2\sum_{n=1}^{\infty}\cos\left(n\pi\frac{z}{L}\right)e^{-\left(\frac{n\pi}{L}\right)^2\alpha t}\right), \tag{9}$$

where q_0 [J m^{-2}] is the absorbed heat energy density in an infinite thin surface layer $\delta(z)$, ρ [kg m^{-3}] is the density, c_p [Jkg^{-1}K^{-1}] the specific heat, α [m^{2}s^{-1}] is the thermal diffusivity and L [m] the sample thickness. In Fig. 3, the temperatures T_{Z22}, calculated with Eq. 9, in reflection as well as in transmission configuration, applying the geometrical and physical properties of Table 1a, are shown. T_{Z33} represents the solution of the 1D heat conduction equation for boundary conditions of the third kind, to demonstrate convective influences.

3.1 Optimum Evaluation Time

The optimum evaluation time is defined by the fact that only time ranges are evaluated which contain information about the heat diffusion inside the sample. If the temperature change reaches an order of magnitude equal to the noise, the signal is truncated at the time t_{end}. This approach also reduces the undesired influence of heat losses due to convection on the measurement result (see T_{Z33} in Fig. 3). The optimum evaluation time is defined with the dimensionless Fourier number: $Fo_{\text{end}} = \alpha\, L^{-2}\, t_{\text{end}}$. For its derivation, we use the signal-to-noise ratio SNR $= T_a/\sigma$, where $T_a = q_0/(\rho c_p L)$ represents the adiabatic temperature. The simulated temperature data T_{Z22} is distorted with a additive white Gaussian noise (AWGN) with a standard deviation σ of 25 mK [21]. To derive an analytical expression for Fo_{end} as a function of the SNR, we utilize an approximation of Eq. 9 with $n = 1$. The dimensionless representation of the approximation is given by

$$\Theta = \frac{T^{n=1}_{Z22}}{T_a} = 1 + 2\cos(\pi z_D)\, e^{-\pi^2\, Fo_{\text{end}}}, \tag{10}$$

with the dimensionless thickness $z_D = \frac{z}{L}$. For $Fo > 0.1$ the approximation with $n = 1$ shows a sufficient agreement with the exact solution to define the cut-off value of the temperature Θ_c for the optimum evaluation time determination:

$$\Theta_c = \begin{cases} 1 - \frac{1}{\text{SNR}} & \text{for } z_D = 1 \text{ (transmission)}, \\ 1 + \frac{1}{\text{SNR}} & \text{for } z_D = 0 \text{ (reflection)}. \end{cases} \tag{11}$$

By substitution of these limit values in Eq. 10, the optimum evaluation time can be determined

$$Fo_{\text{end}} = -\frac{1}{\pi^2}\log\left(\frac{1}{2\ \text{SNR}}\right). \tag{12}$$

3.2 Virtual A-scan Representation

For the derivation of the virtual wave, we use the truncated temperature data $\mathbf{T}^{\text{end}}_{Z22}$, corresponding to the optimum evaluation time (Eq. 12). In Fig. 4, the virtual waves obtained by the regularization techniques T-SVD and ADMM are compared for reflection and transmission configuration. The amplitude of the virtual wave is plotted versus the propagation distance $z = c\,t$, whereby the local maxima of $\mathbf{T}^{\text{T-SVD}}_{\text{virt}}$ and $\mathbf{T}^{\text{ADMM}}_{\text{virt}}$ represent the back wall of the sample. Because the virtual speed of sound c can be chosen arbitrary, we prescribe the dimensionless virtual speed of sound (Eq. 5) to be

$$\tilde{c} = \begin{cases} 1 & \text{for } z_D = 1 \text{ (transmission)}, \\ \frac{1}{2} & \text{for } z_D = 0 \text{ (reflection)}, \end{cases} \tag{13}$$

whereby in reflection configuration $\tilde{c}$ has to be halved because of the two way diffusion.

The analytic virtual wave $\mathbf{T}^{\text{a}}_{\text{virt}}$ is derived by applying the method of images to solve the PDE of the virtual wave equation [9]. Based on the two way diffusion process the back wall echos in reflection configuration result in a lower amplitude than in transmission configuration. The values of the virtual waves based on T-SVD regularization oscillate around 0 K, which makes the evaluation more difficult in contrast to ADMM, where only positive values are allowed. Additionally, the prior information in form of sparsity reduces the full half width of the peaks for $\mathbf{T}^{\text{ADMM}}_{\text{virt}}$, whereby an exact localization of the back wall echos can be achieved.

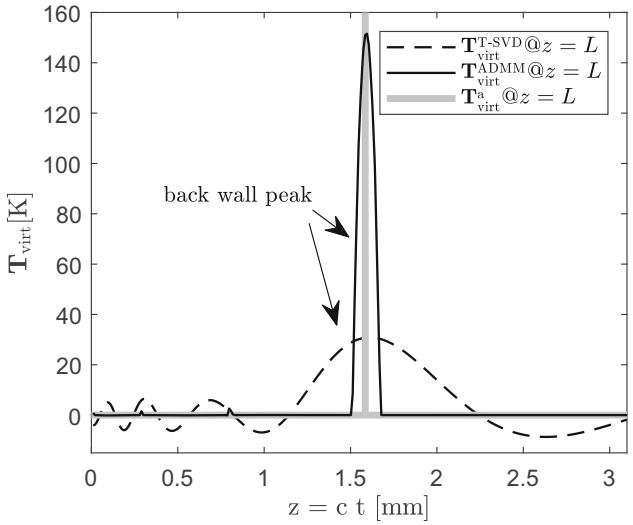

(a) Transmission configuration ($z = L$)

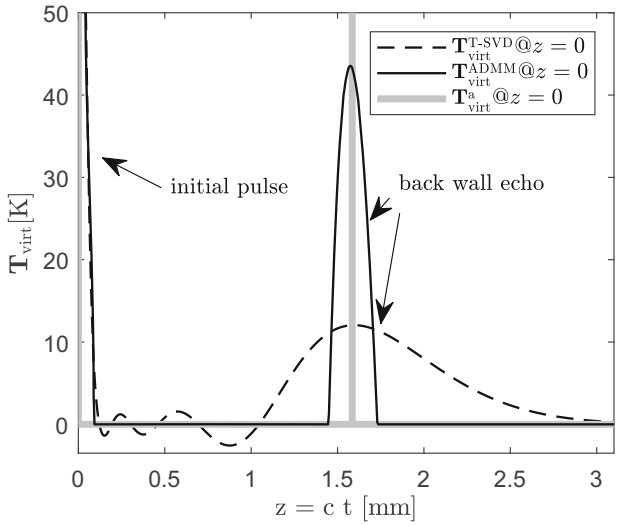

(b) Reflection configuration ($z = 0$)

Fig. 4 A-scan representation of the virtual wave for transmission (**a**) and reflection configuration (**b**), where the amplitude of the virtual waves is plotted versus the propagation distance z. Both (**a**) and (**b**) are calculated with geometrical and physical properties in Table 1a

3.3 Virtual Time-of-Flight Measurements

For the estimation of the thermal diffusion time t_{d}, virtual ToF measurements can be used. If the thermal diffusivity of the examined material is known, the kernel K can be calculated accurately. Depending on spatial variations of the micro-structure, the thermal diffusivity α is unknown and literature based values α_{init} have to be assumed for the initial calculation of the kernel K. We determine the ToF, respectively the position of the back-wall peak, in transmission configuration by measuring the time between the initial pulse and the time when the propagating virtual wave arrives at the back wall (Fig. 4a). In reflection configuration the ToF is determined by measuring the time between the initial pulse and the corresponding echo at the back surface of the sample (Fig. 4b). For the calculation of the virtual waves, shown in Fig. 5, we used two different temperature data sets derived by Eq. 9 from values given in Table 1.

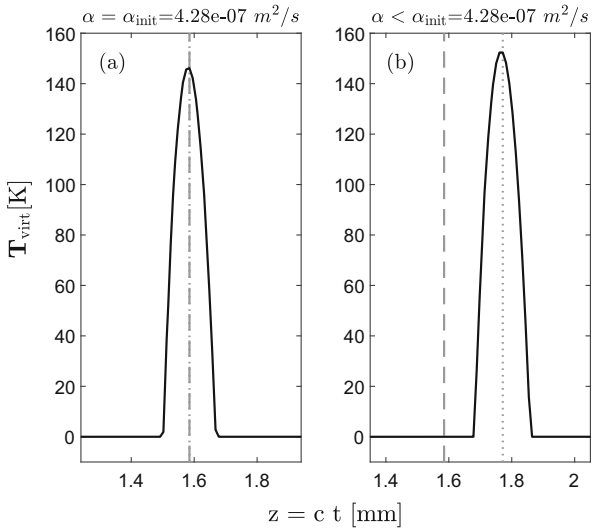

Fig. 5 Dependence of the ToF on the thermal diffusivity α of the examined material (Table 1)

Table 1 Thermophysical [22–24] and geometrical properties used for calculation of T_{Z22} (Eq. 9)

Property		Unit	(a)	(b)
Thermal conductivity	k	W m^{-1} K^{-1}	0.77	0.62
Density	ρ	kg m^{-3}	1500	1500
Heat capacity	c_{p}	Jkg^{-1}K^{-1}	1200	1200
Thermal diffusivity	α	m^{2}s^{-1}	4.28e−7	3.42e−7
Mechanic thickness	L	m	1.59e−3	1.59e−3
Results for validation				
Thermal diffusion time	$t_{\text{d}} = \frac{L^2}{\alpha}$	s	5.907	7.392

We assumed the same initial thermal diffusivity $\alpha_{\text{init}} =$ 4.28e-7 m^{2}s^{-1} for both examinations, whereby in case (a) $\alpha = \alpha_{\text{init}}$ and in case (b) $\alpha < \alpha_{\text{init}}$. The dashed lines in Fig. 5 depict the thickness L and the dotted lines show the estimated thickness L_{est}

$$L_{\text{est}} = N\,\Delta_z \begin{cases} = L & \text{for } \alpha = \alpha_{\text{init}}, \\ > L & \text{for } \alpha < \alpha_{\text{init}}, \end{cases} \tag{14}$$

where Δ_z denotes the spatial resolution and N is the index of $\max(\mathbf{T}_{\text{virt}})$ that corresponds to the estimated back wall peak. The resulting ToF can only be determined correctly, if the thermal diffusivity of the examined material is known $\alpha = \alpha_{\text{init}}$. Substituting $\Delta_z^2/\alpha\big|_{\alpha\,=\,\alpha_{\text{init}}} = \Delta_{t_{\text{d}}}$ in Eq. 5 results in

Table 2 ToF based results for the thermal diffusion time, derived from Fig. 5

Property		Unit	(a)	(b)
Estimated thickness	L_{est}	m	1.585e−3	1.772e-3
Results				
Thermal diffusion time	$t_{\text{d}} = \frac{L_{\text{est}}^2}{\alpha_{\text{init}}}$	s	5.883	7.349

$$\frac{\Delta_{\text{Fo}}}{\Delta_t} = \frac{1}{\Delta_{t_{\text{d}}}} = \text{constant}, \tag{15}$$

whereby the ToF related thermal diffusion time is given by

$$t_{\text{d}} = \frac{(N\Delta_z)^2}{\alpha_{\text{init}}} = \frac{L^2}{\alpha}. \tag{16}$$

For both examples in Fig. 5, independent of prior knowledge of thickness L and thermal diffusivity α the thermal diffusion time t_{d} results given in Table 2.

The difference between the theoretic solution for the thermal diffusion time t_{d} in Table 1 and the experimental solution (Table 2) is less than 1 % and results from discretization.

4 Experimental Results

To demonstrate the applicability of the VWC for parameter estimation in CFRP, two different experiments were performed. The repeatability and accuracy of the VWC is shown with experiments on a step wedge, where the results are compared with state-of-the-art methods. Furthermore, the VWC is applied on different CFRP coupons for porosity estimation. Based on an effective medium theory (EMT), porosity values can be derived, which are validated with 3D X-ray computed tomography measurements.

4.1 Pulsed-Thermography Set-Up

The experimental setup for optical-excited pulsed thermography experiments in reflection as well as in transmission configuration is shown in Fig. 6. Two flash lamps with an electrical energy of 12 kJ and a pulse duration of approx. 2 ms, driven by a signal generator, are used for thermal excitation. The absorbed heat energy density is approximately $q_0 = 11.8$ kJ m^{-2}, which was derived by adapting the theoretical to the experimental adiabatic temperature. The data acquisition is triggered by a PC and timed to the excitation signal, whereby the temperature measurements were carried out with an IR camera equipped with an indium antimonide (lnSb) detector. The cooled 1280 × 1024 pixel focal plane array camera has a NETD of about 25 mK and is sensitive in a spectral range of 1.5–5.1 microns. The spatial resolution

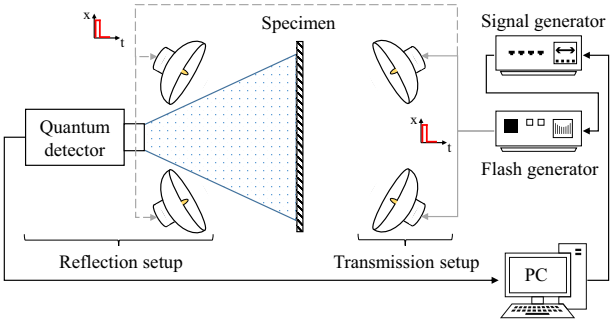

Fig. 6 Scheme of the measurement setup for transmission (grey solid line) and reflection (grey dashed line) configuration with flash excitation

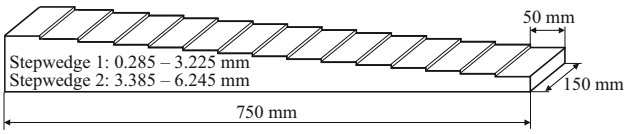

Fig. 7 Scheme of the CFRP step wedge sample

of the measurements in both experiments was 0.4 mm per pixel.

4.2 Reference Measurements on a CFRP Step Wedge

4.2.1 Test Specimen

For the validation of the VWC on heterogeneous material we examine two step wedges (each 15 steps), made from plain epoxy based woven fabric CFRP (Fig. 7), with transverse isotropic material behaviour [25].

The samples are not porous ($\Phi = 0$), thereby their thermophysical properties are only dependent to the thermophysical properties of the matrix material (fibre and resin). Since there are no porosity dependent microstructural variations, the thermal diffusivity α is assumed to be constant for all steps. The whole size of the step wedges in lateral direction is (750 × 150) mm^2 and the corresponding size to one step is (50 × 150) mm^2. Five steps, with a thickness from $L = 1.59$ mm up to $L = 4.86$ mm, are examined.

4.2.2 Measurement Parameters

For the experimental evaluation of the thermal diffusion time t_{d}, the width of the discrete time step Δt, respectively the frames per second (FPS) were chosen in dependence of the specimen thickness. The final measurement time is equal to the characteristic diffusive time scale $t_{\text{N}} = t_{\text{d}}$ corresponding to Fourier number $Fo = 1$. The characteristic diffusive time scale $t_{\text{d}} = L/\alpha^2$ describes a long-time conduction regime, where the temperature in the body reached the adiabatic

Table 3 Measurement parameters for the pulsed thermography experiments in dependence of the step wedge thickness

#	L mm	$t_{\mathrm{N(Fo=1)}}$ s	FPS $\approx 1/\mathrm{t}$ 1/s
7	1.59	5.88	170
11	2.40	13.32	75
15	3.23	24.37	41
19	3.99	37.00	27
23	4.86	55.50	18

plateau T_{a}. Under the initial assumption to have the same number of data points ($N = 1000$) for each step of the step wedge, the discrete time step Δ_t results in Table 3.

For further data processing, due to the truncation of the measurement data (Eq. 12), only time ranges are evaluated which contain information about the heat diffusion inside the sample. In addition, the influence of heat losses due to convection on the measurement results is reduced. The width of the discrete spatial steps was chosen such that the reconstruction area corresponds to four times the thickness of the component: $\Delta z = 4L/(N \cdot Fo_{\mathrm{end}})$. Thus ensures for each measurement nearly the same number of data points ($N_{\mathrm{Fo_{end}}} = N \cdot Fo_{\mathrm{end}}$), in dependence to the SNR. Since the truncated measurement data and the dimension of the kernel $\mathbf{K} \in \mathbb{R}^{\mathrm{N_{Fo_{end}}} \times \mathrm{N_{Fo_{end}}}}$ are dependent on the number of remaining discretizations, the computational costs are reduced due to $Fo_{\mathrm{end}} < 1$. The used regularization technique ADMM is designed for filtering noise based influence to the inverted solution [26]. We assume the experimental noise for each single position $\mathbf{r}$ in every measurement is nearly constant. For acceleration of the regularization operation we use a global regularization parameter. It is determined at position $\mathbf{r}(1, 1)$ and used in every position $\mathbf{r}$. We take into account 72 pixels per step for the calculation of the mean value and standard deviation.

4.2.3 Results for Validation of the Method

The result of the inverse problem (Eq. 3) is directly dependent on the thermal measurement, so the truncated experimental temperatures $\mathbf{T}_{\mathrm{meas}}$ are analysed and compared to the regularized temperature

$$\mathbf{T}_{\mathrm{reg}}^{\mathrm{ADMM}} = \mathbf{K}\mathbf{T}_{\mathrm{virt}}, \tag{17}$$

for model validation purposes. In Fig. 8 the measured temperatures on the back-side (Fig. 8a) and on the front-side (Fig. 8b) are shown for five different steps # = [7, 11, 15, 19, 23], as these steps cover nearly the entire range of the step wedge.

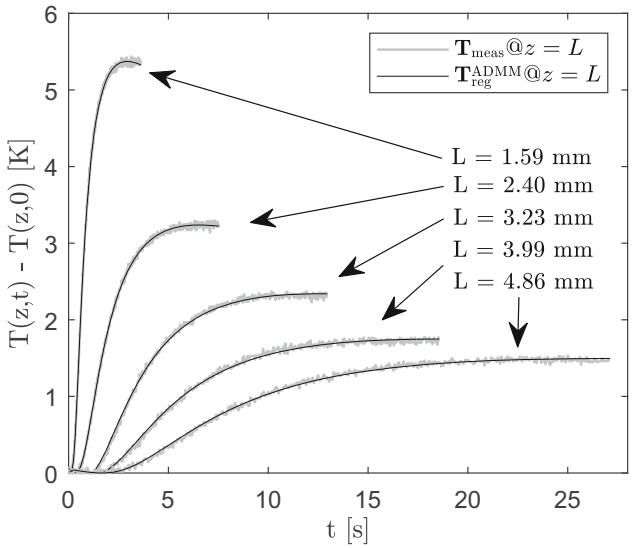

(a) Transmission configuration ($z = L$)

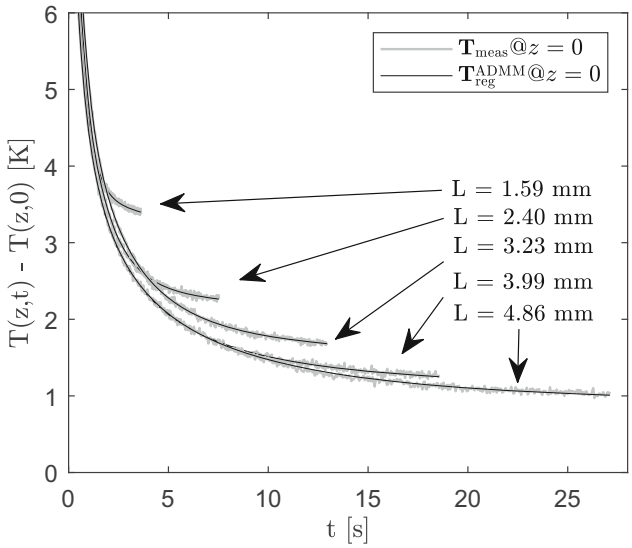

(b) Reflection configuration ($z = 0$)

Fig. 8 Comparison of the experimental $\mathbf{T}_{\mathrm{meas}}$ and regularized temperatures $\mathbf{T}_{\mathrm{reg}}^{\mathrm{ADMM}}$ for five different steps # = [7, 11, 15, 19, 23]. The measurement parameters are given in Table 3

The comparison of the measured temperature values $\mathbf{T}_{\mathrm{meas}}$ (for only one pixel each step) to the regularized temperatures $\mathbf{T}_{\mathrm{reg}}^{\mathrm{ADMM}}$ show good agreement and demonstrate the filter effect due to regularization. Based on virtual ToF measurements we estimate the thermal diffusion time t_{d} in transmission (Fig. 9a) and reflection configuration (Fig. 9b) whereby the results are plotted versus the thickness L, shown in Fig. 9.

In both examination configurations the VWC is compared to respective state-of-the-art methods, the Linear Diffusivity Fitting (LDF) method [27,28] und Thermographic Signal Reconstruction (TSR) [29,30]. The dashed lines show a quadratic fit whereby the fitting parameter, the diffusiv-

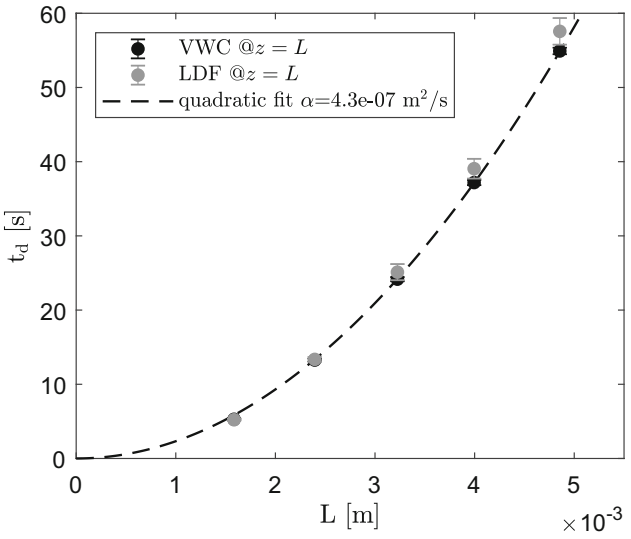

(a) Transmission configuration ($z = L$)

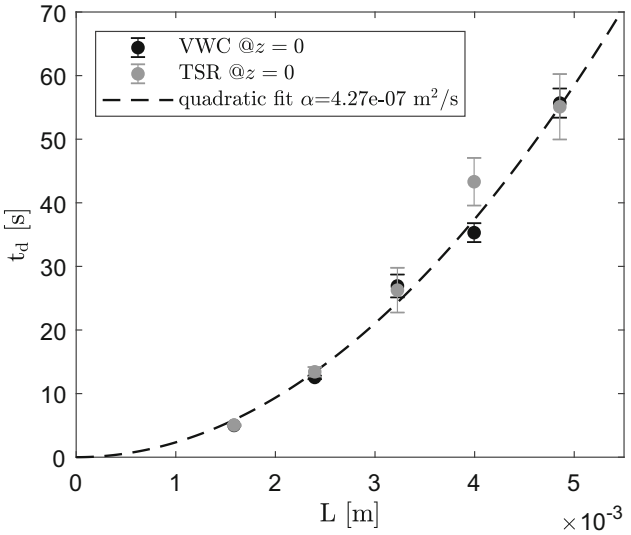

(b) Reflection configuration ($z = 0$)

Fig. 9 Estimated diffusion time t_d for five different steps # = [7, 11, 15, 19, 23], in comparison with state-of-the-art methods for transmission (LDF) and reflection configuration (TSR)

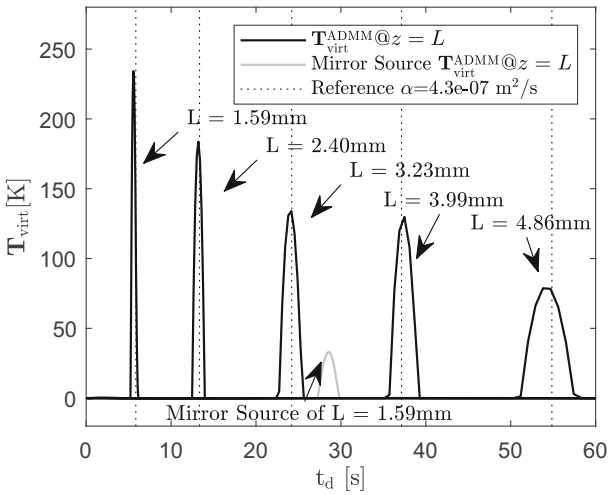

(a) Transmission configuration ($z = L$)

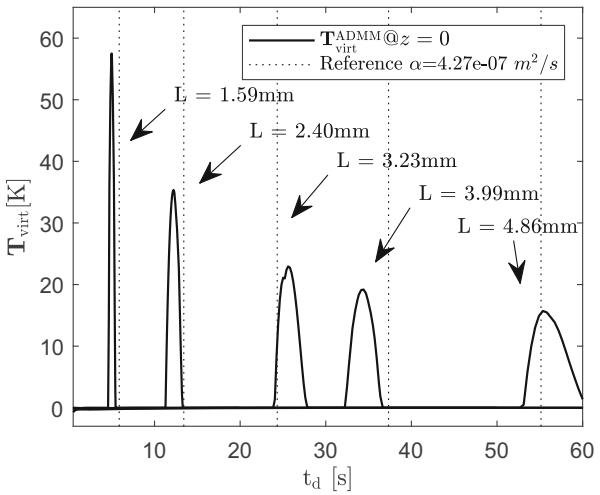

(b) Reflection configuration ($z = 0$)

Fig. 10 A-scan representation of the virtual wave, where the amplitude of the virtual waves is plotted versus the thermal diffusion time t_d for the steps # = [7, 11, 15, 19, 23]

ity α, was determined based on VWC results. The fitting parameters in transmission and reflection configuration are nearly equal and correspond to literature based values for non-porous CFRP (Φ=0). For transmission configuration the averaged standard deviation of the thermal diffusion time over five steps is 1.1% in comparison to the LDF with 3%. In reflection configuration a significant improvement of the standard deviation of the estimated thermal diffusion times is shown. Due to the large scattering of the thermal diffusion times estimated by TSR, where the experimental log-log thermogram is fitted by a logarithmic polynomial of degree n=9 [30], no quantitative porosity estimation was possible, as also concluded by Mayr et al. [6]. For all TSR evaluations, the measurement data $\mathbf{T}_{meas}$ was not truncated and the full temporal data ($Fo = 0.05$ - $Fo = 1$) was used for evaluation. Despite the doubled diffusion process through the material in reflection configuration the standard deviation of the estimated thermal diffusion time, carried out by the VWC, is also less than 4 % and therefore more accurate than the state-of-the-art method TSR. In Fig. 10 the A-Scan representation of the virtual waves for the examined steps is shown. The solution of the inverse problem was calculated for every position **r** where the depicted virtual waves represent the spatial averaged $\mathbf{T}_{virt}^{ADMM}$ for 72 pixels in transmission configuration (Fig. 10a) and in reflection configuration (Fig. 10b). In order to gain the correct ToF, respectively the thermal diffusion time t_d, for the A-Scan representation we assumed for the respective initial thermal diffusivity α_{init} the prior determined spatial averaged thermal diffusivity α for each step. The given reference lines are based on the determined fitting

parameter α (Fig. 9) and represent the nominal value of the thermal diffusion time for the examined step. The amplitude of the virtual wave decreases with increasing thickness of the sample. For high thicknesses, due to increasing peak width despite a fixed number (transmission configuration I = 200 and reflection configuration I = 400) of regularization iterations, the error in the estimation of the thermal diffusion time increases. In heat diffusion the wavenumber k corresponds to the thermal diffusion length μ

$$k = \frac{2\pi}{\lambda_{\mathrm{PT}}} = \frac{1}{\mu}, \tag{18}$$

for $\mu = L$ follows a wavelength $\lambda_{\mathrm{PT}} = 1.26\text{e-}2$ m for a thickness $L = 2$ mm for example. Since such high values of λ_{PT} correspond to the thickness of tens of plies, with the strongly damped thermal waves, no interlaminar interface echos, known from ultrasonic testing ($\lambda_{\mathrm{UT}} \approx \lambda_{\mathrm{PT}}/100$ for testing frequency of 5 MHz), occur when investigating heterogeneous materials. In photothermal testing, the test specimen can be treated as a homogeneous material as you can only detect the front and back-wall echos. The prior information of sparsity is feasible for regularization.
These validation measurements on CFRP step wedges, demonstrate reliable results of high accuracy in estimating the thermal diffusion time t_{d}. Thus allows a suitable quantitative porosity estimation of heterogeneous materials, based on thermal diffusion time measurements in transmission as well as in reflection configuration.

4.3 Porosity Estimation on CFRP Coupons

4.3.1 Test Specimen

For quantitative porosity estimation in CFRP we examine 31 calibrated prepreg porosity coupons, made from plain epoxy based woven fabric, with a different amount of plies $N = [5, 10, 20]$ (Fig. 11). The size of the coupons in lateral direction is (40×20) mm^2 and the thickness of the specimen depends on porosity Φ

$$L(\Phi) = L_0 \frac{1}{1-\Phi}, \tag{19}$$

for a specific amount of plies N where $L_0 = N l_{\mathrm{x}}$ is the nominal specimen thickness without porosity ($\Phi = 0$) and $l_{\mathrm{x}} = 0.216$ mm represents the nominal ply thickness of one laminae. The nominal coupon thickness varies from 1.08 mm (5 plies) to 4.32 mm (20 plies). Cone beam X-ray computed tomography (XCT) and image analysis were carried out to obtain the microstructure in a representative volume of porous CFRP.

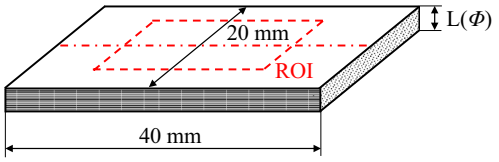

Fig. 11 Scheme of the porosity coupons with the region of interest used for the porosity evaluation

Table 4 Measurement parameters for the pulsed thermography experiments in dependence of the porosity coupon thickness (5-, 10- and 20-ply material)

#	L_{min} mm	L_{max} mm	L_{avg} mm	$t_{\mathrm{N(Fo=1)}}$ s	FPS $\approx$ 1/t 1/s
5-ply	0.90	1.22	1.07	5.81	172
10-ply	1.92	2.58	2.17	9.34	107
20-ply	4.24	5.29	4.56	37	27

4.3.2 Measurement Parameters

The temporal discretization, respectively the frames per second (FPS), was determined by using the thickness information in Table 4 in exactly the same way as for the validation of the method in Sect. 4.2.2.

For the 5-ply material, based on the size of the observation window of the IR-Camera, the desired measuring frequency of FPS = 373 1/s could not be reached due to hardware limitations, so the maximal possible measuring frequency corresponding to the observation window size was chosen. To evaluate only time ranges containing heat diffusion information and to reduce the influence of heat losses due to convection, we truncate the measurement data corresponding to the optimum evaluation time (Eq. 12). For the correct temporal truncation of the porosity affected samples in reflection configuration we used the already, in transmission configuration, estimated diffusion times t_{d}. To prevent failure due to edge effects, a region of interest (ROI) with a size of 11×31 pixel was processed for the calculation of the mean value and standard deviation of the thermal diffusion time. In contrast to the measurements on the step wedge, we do not use positivity as prior information for regularization to determine the virtual wave in reflection mode from porous samples. The reason for this is that high-frequency thermal waves also contribute to the measured temperature curves, especially in the short-term range. The high-frequency thermal waves are scattered and reflected at near-surface pores and thereby influence the resulting surface temperature. This means that the necessary scale separation for the assumption of an effective medium is no longer given and so a multidimensional heat flux must be considered and the restriction of only positive values of the virtual wave is not more valid.

Table 5 Thermophysical properties of the CFRP constituents used for the effective medium approximation [32,33]

Property		Unit	Matrix	Pore
Thermal conductivity	k	$W\,m^{-1}\,K^{-1}$	0.7	0.026
Density	ρ	$kg\,m^{-3}$	1570	1.2
Heat capacity	c	$Jkg^{-1}K^{-1}$	1200	1000
Thermal diffusivity	α	$m^2\,s^{-1}$	3.72e-7	2.17e-5

In contrast to that, in transmission configuration the sample acts as a low pass filter and only low frequency components of the thermal waves contributes to the measured temperature data. So, in transmission mode the assumption of positivity can also be used for measurement data of porous CFRP.

4.3.3 Effective Medium Theory

For a quantitative determination of porosity, based on thermal diffusion times t_d estimated by ToF it is imperative to use a material model based on EMT. Since the thickness L (Eq. 19) and the effective thermal diffusivity α_{eff} is affected by porosity Φ we apply the model for the nominal thermal diffusion time, derived in Appendix 1

$$t_d(\Phi) = \frac{L_0^2}{\alpha_{app}} = \frac{(Nl_x)^2}{(\alpha_0 + \alpha_1\Phi)(1-\Phi)^2}, \tag{20}$$

which enables modeling without information of the actual sample thickness $L(\Phi)$. α_0 is the thermal diffusivity of the void-free matrix and α_1 is the sensitivity coefficient which represents the change of the effective thermal diffusivity due to the change of the porosity in dependence on the averaged pore shape. The used value $\alpha_0 = 0.374\ mm^2\,s^{-1}$ can be derived by a measurement of a void free ($\Phi = 0$) CFRP coupon and $\alpha_1 = -0.673\ mm^2\,s^{-1}$ is derived by a Mori–Tanaka Approximation [25,31] using the thermophysical properties in Table 5.

4.4 Results of Porosity Estimation

For demonstration of statistical uniform distribution of the pores, in a first instance diffusion time images (Fig. 12) for three 20-ply porosity coupons with different porosity values $\Phi = [1.55\ \%, 5.62\ \%, 10\ \%]$ are processed exemplary.

We used the truncated experimental temperatures $\mathbf{T}_{meas}$ and applied the pixel-wise, ToF based, estimation of the thermal diffusion time t_d. Along the dash-dot lines line profiles of the determined thermal diffusion times are depicted in Fig. 12, to obtain an expressive representation of the homogeneity of the samples. The region of interest for the further calculation of mean values and standard deviations,

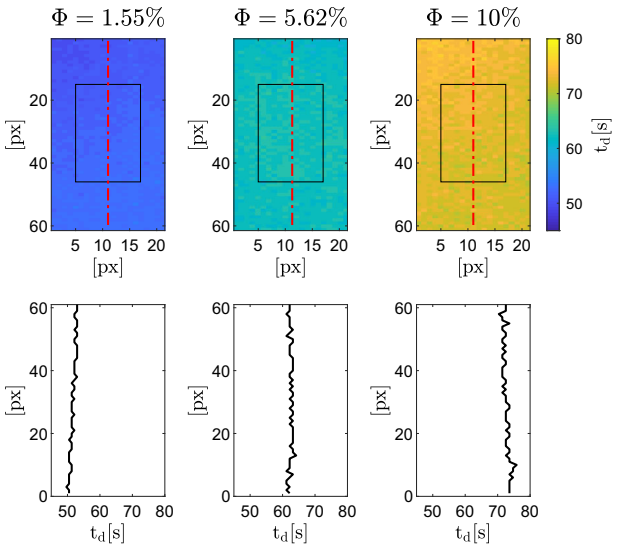

Fig. 12 Comparison of 20-plies CFRP diffusion time images for transmission configuration, with different porosity (Φ = 1.55% to 10%)

is marked by a black rectangle (11 × 31 pixel). In total we examined 31 calibrated porosity coupons with porosity up to 10%. Previous Cone-beam XCT measurements with a resolution of $(10\mu m)^3$ have been used for characterization of the microstructure for EMT modelling and to gain a reference porosity value. The pores were determined by a segmentation method [34,35] that separates pore and matrix material, whereby only pores with a volume greater than 27 voxels (corresponding to a sphere equivalent diameter from $37.2\mu m$) were considered.

The resulting spatial mean values and the standard deviations of the estimated thermal diffusion times t_d for each single coupon are illustrated logarithmically in Fig. 13 versus the porosity value, derived by XCT (Φ = 0% to 10%).

The model for the nominal thermal diffusion time (Eq. 20), based on EMT, is represented by dashed lines for 5-, 10-, and 20-ply material. With increasing thickness (number of plies) the thermal diffusion time increases and with a given number of layers it increases for higher porosity values. The estimated thermal diffusion times from experimental data correspond to the predicted values, derived by EMT, quite well. The overall uncertainty for a photothermal porosity estimation by thermal diffusion times from VWC is less than $\Phi = \pm 0.8\ \%$ in transmission configuration. In addition to transmission configuration, a reliable porosity estimation based on the novel approach of virtual ToF measurements for thermographic data, can also be performed quickly and with good accuracy for reflection configuration measurements. Due to the double diffusion process in reflection configuration the standard deviation is slightly larger whereby the overall uncertainty is less than $\Phi = \pm 1.5\ \%$.

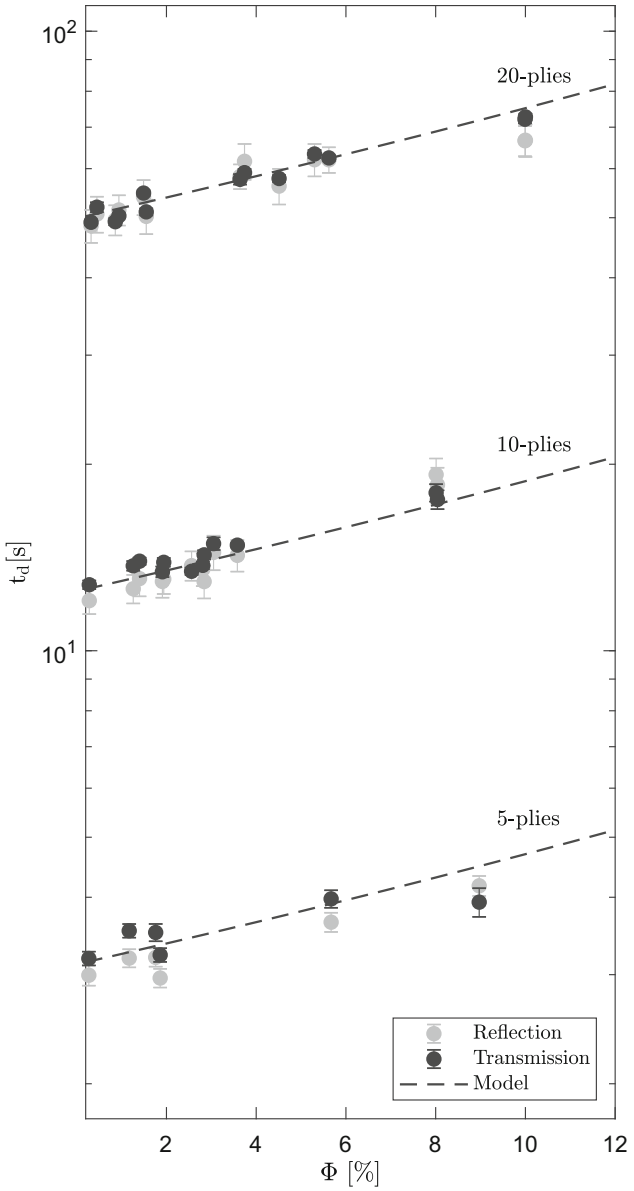

Fig. 13 The measured diffusion time t_d versus porosity Φ for flash excited 5-, 10- and 20-ply porosity coupons. The dashed line shows the examined material model

4.5 Conclusion and Outlook

In this paper, we apply the Virtual Wave Concept on CFRP for the estimation of the porosity-dependent thermal diffusion time from flash-excited pulsed thermography experiments. Considering a novel, SNR dependent, approach for the temporal truncation of measurement data only time ranges which contain information about the heat diffusion inside the sample are evaluated. In addition this optimum evaluation time also ensures the reduction of undesired influences by convection. Due to the VWC, pulse-echo and through-transmission method are applicable for the Time-of-Flight determination of a virtual wave corresponding to the truncated photothermal measurements. For the calculation of the virtual wave field a local transformation is applied to the temperature data, whereby this transformation is an ill-posed 1D heat conduction problem. To gain an appropriate solution, the ADMM is used for regularization, which allows the inclusion of prior information. We assume positivity due to 1D heat diffusion and a sparse virtual wave field, based on the assumption of an effective medium. This assumptions lead to virtual waves containing only positive values and sharp peaks, which allow the exact localization of the back wall echo.

After reference measurements on a CFRP step wedge, where an improvement of the standard deviation compared to state-of-the-art methods in transmission and reflection configuration is shown, the VWC is applied for quantitative porosity estimation. A model for the nominal thermal diffusion time is derived from an effective medium theory based linear model for effective thermal diffusivity. The model is validated with the aid of a large number of porosity coupons. It is shown that the results of the photothermal porosity estimation by the Virtual Wave Concept match the porosity determined by cone beam X-ray computed tomography reference measurements quite well. The overall uncertainty for photothermal porosity estimation from VWC is highly improved for reflection configuration, since the standard deviation of the estimated thermal diffusion times is more accurate than state-of-the-art methods. Owing these improved reflection configuration results, a future, fast and non-contacting quantitative porosity estimation from thermographic measurements will be possible even for complex shapes and hybrid structures.

Acknowledgements Open access funding provided by University of Applied Sciences Upper Austria. The main financial support by the Austrian Federal Ministry of Science, Research and Economy and the National Foundation for Research, Technology and Development is gratefully acknowledged. Furthermore, the study has been supported by the following projects and funding agencies: the project "SpaceNDT" funded by the FFG in the framework of ASAP14, the project "multimodal and in-situ characterization of inhomogeneous materials" (MiCi) funded by the federal government of Upper Austria and the European Regional Development Fund (EFRE) in the framework of the EU-program IWB2020, the strategic economic-research program "Innovative Upper Austria 2020" of the province of Upper Austria and financial support was also provided by Smarter Processes (PSSP)" (Contract # 871974). This programme is promoted by BMVIT, BMDW, the federal state of Upper Austria and the federal state of Styria, represented by SFG.

Funding Open access funding provided by University of Applied Sciences Upper Austria.

Appendix: Nominal Thermal Diffusion Time Model

The model for the nominal thermal diffusion time, given in Eq. 20, is derived from the EMT based, linear model for effective thermal diffusivity

$$\alpha_{\text{eff}} = \alpha_0 + \alpha_1 \Phi, \tag{A.1}$$

proposed by Mayr et al. [7]. Whereby in case of porosity ($\Phi > 0$) the effective thermal diffusivity

$$\alpha_{\text{eff}} = \frac{k_{\text{eff}}}{(\rho c)_{\text{eff}}}, \tag{A.2}$$

decreases where k_{eff} is the effective heat conduction and $(\rho c)_{\text{eff}}$ the effective volumetric heat capacity, both describing a quasi-homogeneous material. The thermal diffusion time is given by $t_{\text{d}} = L(\Phi)^2/\alpha_{\text{eff}}$ whereby the thickness $L(\Phi)$ (Eq. 19) and the thermal diffusivity α_{eff} is affected by porosity Φ. To determine the effective thermal diffusivity α_{eff} from the measured thermal diffusion time t_{d} the knowledge of the actual sample thickness is mandatory and vice versa. A suitable way for modeling the porosity affected thermal diffusion time

$$t_{\text{d}} = \frac{L(\Phi)^2}{\alpha_{\text{eff}}} = \frac{L_0^2}{\alpha_{\text{app}}}, \tag{A.3}$$

results in the apparent thermal diffusivity α_{app}, where is no need for the knowledge of the actual thickness of the sample. Taking into account the porosity dependent thickness change (Eq. 19) and the linear model for effective thermal diffusivity (Eq. A.1) the apparent thermal diffusivity is given

$$\alpha_{\text{app}} = \alpha_{\text{eff}} \left(\frac{L_0}{L}\right)^2 = (\alpha_0 + \alpha_1 \Phi)(1 - \Phi)^2 \tag{A.4}$$

by substituting Eq. A.4 into Eq. A.3 results in

$$t_{\text{d}}(\Phi) = \frac{(N l_{\text{x}})^2}{(\alpha_0 + \alpha_1 \Phi)(1 - \Phi)^2}. \tag{A.5}$$

References

1. Campbell, F.C.: Structural Composite Materials. ASM International, Materials Park (2010)
2. Olivier, P., Cottu, J.P., Ferret, B.: Effects of cure cycle pressure and voids on some mechanical properties of carbon/epoxy laminates. Composites **26**(7), 509–515 (1995). https://doi.org/10.1016/0010-4361(95)96808-J
3. Costa, M.L., Almeida, S.F.M., Rezende, M.C.: The influence of porosity on the interlaminar shear strength of carbon/epoxy and carbon/bismaleimide fabric laminates. Compos. Sci. Technol. **61**(14), 2101–2108 (2001). https://doi.org/10.1016/S0266-3538(01)00157-9
4. Balageas, D., Maldague, X., Burleigh, D., Vavilov, V.P., Oswald-Tranta, B., Roche, J.M., Pradere, C., Carlomagno, G.M.: Thermal (ir) and other ndt techniques for improved material inspection. J. Nondestruct. Eval. **35**(1), 18 (2016). https://doi.org/10.1007/s10921-015-0331-7
5. Toscano, C., Meola, C., Carlomagno, G.M.: Porosity distribution in composite structures with infrared thermography. J. Compos. **2013**, 1–8 (2013). https://doi.org/10.1155/2013/140127
6. Mayr, G., Plank, B., Gruber, J., Sekelja, J., Hendorfer, G.: Quantitative evaluation of the effective thermal diffusivity for model-based porosity prediction in cfrp. Quant. InfraRed Thermogr. J. **13**(1), 70–82 (2016). https://doi.org/10.1080/17686733.2015.1093310
7. Mayr, G., Gresslehner, K.H., Hendorfer, G.: Non-destructive testing procedure for porosity determination in carbon fibre reinforced plastics using pulsed thermography. Quant. InfraRed Thermogr. J. **14**(2), 263–274 (2017). https://doi.org/10.1080/17686733.2017.1326078
8. Cernuschi, F.: Can tbc porosity be estimated by non-destructive infrared techniques? A theoretical and experimental analysis. Surf. Coat. Technol. **272**, 387–394 (2015). https://doi.org/10.1016/j.surfcoat.2015.03.036
9. Mayr, G., Stockner, G., Plasser, H., Hendorfer, G., Burgholzer, P.: Parameter estimation from pulsed thermography data using the virtual wave concept. NDT E Int. **100**, 101–107 (2018). https://doi.org/10.1016/j.ndteint.2018.09.003
10. Thummerer, G., Mayr, G., Hirsch, P.D., Ziegler, M., Burgholzer, P.: Photothermal image reconstruction in opaque media with virtual wave backpropagation. NDT E Int. (2020). https://doi.org/10.1016/j.ndteint.2020.102239
11. Thummerer, G., Mayr, G., Haltmeier, M., Burgholzer, P.: Photoacoustic reconstruction from photothermal measurements including prior information. Photoacoustics (2020). https://doi.org/10.1016/j.pacs.2020.100175
12. Burgholzer, P., Thor, M., Gruber, J., Mayr, G.: Three-dimensional thermographic imaging using a virtual wave concept. J. Appl. Phys. **121**(10), 105102 (2017). https://doi.org/10.1063/1.4978010
13. Pozrikidis, C.: Fluid Dynamics: Theory, Computation, and Numerical Simulation, 3rd edn. Springer, New York (2017)
14. Burgholzer, P., Hendorfer, G.: Limits of spatial resolution for thermography and other non-destructive imaging methods based on diffusion waves. Int. J. Thermophys. **34**, 1617–1632 (2013). https://doi.org/10.1007/s10765-013-1513-0
15. Burgholzer, P.: Thermodynamic limits of spatial resolution in active thermography. Int. J. Thermophys. **36**(9), 2328–2341 (2015). https://doi.org/10.1007/s10765-015-1890-7
16. Wang, L.V.: Photoacoustic Imaging and Spectroscopy, Optical Science and Engineering, vol. 144. CRC Press, Boca Raton (2009)
17. Aster, R.C., Borchers, B., Thurber, C.H.: Parameter Estimation and Inverse Problems, 3rd edn. Elsevier, Amsterdam (2019)
18. Hansen, P.C.: Analysis of discrete ill-posed problems by means of the l-curve. SIAM Rev. **34**(4), 561–580 (1992). https://doi.org/10.1137/1034115

19. Krautkrämer, J., Krautkrämer, H.: Ultrasonic Testing of Materials. Springer, Berlin (1990)
20. Cole, K.D., Beck, J.V., Haji-Sheikh, A., Litkouhi, B.: Heat Conduction Using Green's Functions. Series in Computational and Physical Processes in Mechanics and Thermal Sciences, 2nd edn. CRC Press, Boca Raton (2011)
21. Breitwieser, S., Zauner, G., Mayr, G.: Characterization of mid-wavelength quantum infrared cameras using the photon transfer technique. Infrared Phys. Technol. (2020). https://doi.org/10.1016/j.infrared.2020.103283
22. Maldague, X.P.V.: Nondestructive Evaluation of Materials by Infrared Thermography. Springer, London (1993)
23. Zalameda, J.N., Winfree, W.P.: Thermal diffusivity measurements on composite porosity samples. In: Thompson, D.O., Chimenti, D.E. (eds.) Review of Progress in Quantitative Nondestructive Evaluation, pp. 1541–1548. Springer, Boston (1990)
24. Connolly, M.P.: The measurement of porosity in composite materials using infrared thermography. J. Reinf. Plast. Compos. **11**(12), 1367–1375 (1992). https://doi.org/10.1177/073168449201101203
25. Torquato, S.: Random Heterogeneous Materials: Microstructure and Macroscopic Properties, Interdisciplinary Applied Mathematics, vol. 16. Springer, New York (2002)
26. Hansen, P.C.: Discrete Inverse Problems: Insight and Algorithms. Fundamentals of Algorithms. SIAM, Philadelphia, PA (2010)
27. Hendorfer, G., Mayr, G., Zauner, G., Haslhofer, M., Pree, R.: Quantitative determination of porosity by active thermography. In: AIP Conference Proceedings 30 July–4 August 2007, pp. 702–708. https://doi.org/10.1063/1.2718039
28. Mayr, G., Plank, B., Sekelja, J., Hendorfer, G.: Active thermography as a quantitative method for non-destructive evaluation of porous carbon fiber reinforced polymers. NDT E Int. **44**(7), 537–543 (2011). https://doi.org/10.1016/j.ndteint.2011.05.012
29. Shepard, S.M.: System for generating thermographic images using thermographic signal reconstruction: United States patent (2004)
30. Balageas, D.: Thickness or diffusivity measurements from front-face flash experiments using the tsr (thermographic signal reconstruction) approach. In: Proceedings of the 2010 International Conference on Quantitative InfraRed Thermography. QIRT Council (2010). https://doi.org/10.21611/qirt.2010.011
31. Mori, T., Tanaka, K.: Average stress in matrix and average elastic energy of materials with misfitting inclusions. Acta Metall. **21**(5), 571–574 (1973). https://doi.org/10.1016/0001-6160(73)90064-3
32. Johnson, W.S., Masters, J.E., Wilson, D.W., Zalameda, J.N.: Measured through-the-thickness thermal diffusivity of carbon fiber reinforced composite materials. J. Compos. Technol. Res. **21**(2), 98 (1999). https://doi.org/10.1520/CTR10951J
33. Rolfes, R.: Transverse thermal conductivity of cfrp laminates: a numerical and experimental validation of approximation formulae. Compos. Sci. Technol. **54**(1), 45–54 (1995). https://doi.org/10.1016/0266-3538(95)00036-4
34. Kerrisk, J.F.: Thermal diffusivity of heterogeneous materials. J. Appl. Phys. **42**(1), 267–271 (1971). https://doi.org/10.1063/1.1659581
35. Plank, B., Sekelja, J., Mayr, G., Kastner, J.: Porositätsbestimmung in der flugzeugindustrie mittels röntgen-computertomografie. Proc. Ind. Comput. Facht. **2010**, 25–34 (2010)